

COMPUTATION OF BLOOD FLOWS ACCOUNTING FOR RED-BLOOD CELL AGGREGATION/FRAGMENTATION

A.S. Kane, Y. Bourgault, A. Iolov
Dept. of Mathematics and Statistics
University of Ottawa
Ottawa ON, K1N 6N5 Canada
akane@uottawa.ca, ybourg@uottawa.ca

R.G.Owens
Dép. de mathématiques et de statistique
Université de Montréal
Montréal QC, H3C 3J7 Canada
owens@DMS.UMontreal.CA

A. Fortin
Dép. de mathématiques et de statistique
Université Laval
Québec QC, G1V 0A6 Canada
afortin@giref.ulaval.ca

ABSTRACT

This article presents flows computed in non-trivial geometries while accounting for the contribution of the red cells to the Cauchy stress using the haemorheological model of Owens (2006), Owens and Fang (2006). In this model the local shear viscosity is determined in terms of both the local shear rate and the average rouleau size, with the latter being the solution of an advection-reaction equation. The model describes the viscoelastic, shear-thinning and hysteretic behaviour of flowing blood, and includes non-local effects in the determination of the blood viscosity and stresses. We present numerical results for a two dimensional aneurytic channel under both steady and pulsatile flow conditions. We compare the flows for two sets of physiologically relevant Reynolds and Deborah numbers. A 3-D flow in a section of a patient-specific carotid artery is also presented.

1 Introduction

Aneurysm rupture incurs high rates of mortality. A detailed understand of the local haemodynamics is vital to the accurate prediction of aneurysm ruptures. Among several approaches, the mathematical investigation of blood flows may help understand the mechanisms behind the growth and rupture of aneurysms. As stagnant flows are commonly seen in aneurysms, the variation of blood viscosity must be properly accounted for. Several rheological models for blood have been proposed in the literature. Almost all of them express the blood viscosity as an explicit function of the local shear rate, whereas much of the blood viscosity that is connected to the shear rate is, in fact, dependent upon the fragmentation and aggregation of the red blood cells (RBC) into rouleaux as the shear stresses on these microstructures change (Owens, 2006). Since these reversible processes occur over time scales that may be large compared with those of the shear rate, the change of viscosity with shear-rate is not instantaneous as would be

predicted by models of the generalised Newtonian or Casson type, for example. In this paper, we will present numerical simulations of blood flows in non-trivial geometries while accounting for the contribution of the RBC to the Cauchy stress using the haemorheological model of Fang and Owens (2006) and Owens (2006). In this model the local shear viscosity is determined in terms of both the local shear rate and the average rouleau size, with the latter being the solution of an advection-reaction equation. The model describes the viscoelastic, shear-thinning and hysteresis behaviour of flowing blood, and includes non-local effects in the determination of the blood viscosity and stresses.

The paper is organised as follows: In Section 2, the non-Newtonian model is briefly introduced and numerical methods are sketched. In Section 3, we present numerical results in a two-dimensional aneurytic channel under both steady and pulsatile flow conditions, and results for steady flows in a three-dimensional human carotid artery.

2 A MESOSCOPIC MODEL FOR BLOOD

2.1 Governing equations

In a macroscopic description of the mechanical properties of flowing blood the primary variables of interest are the velocity, denoted by \mathbf{u} , the pressure, denoted by p , and the extra stress $\boldsymbol{\sigma}$, due to viscous and elastic forces. Assuming that RBC can aggregate to form rouleaux but their density is fixed in our model, the blood is then incompressible and conservation of mass reads as

$$\nabla \cdot \mathbf{u} = 0 \quad (1)$$

The forces acting on the fluid can be decomposed into body forces, \mathbf{f} , such as gravity and those due to the pressure and

extra stress, p and σ . Balance of linear momentum then gives,

$$\rho_f \frac{Du}{Dt} = -\nabla p + \nabla \cdot \sigma + f \quad (2)$$

where ρ_f is the fluid density and $\frac{Du}{Dt}$ denotes the material derivative of u . The macroscopic descriptions of incompressible fluids differ according to the constitutive equation satisfied by the extra stress tensor σ . The most fundamental case, viz. Newtonian fluids, expresses σ as being proportional to the rate of deformation tensor, $\dot{\gamma}(u) := \frac{1}{2}(\nabla u + \nabla u^T)$. Although the linear relationship between the extra stress tensor and the rate of deformation tensor is adequate for simple fluids such as water or air, it fails to be so for microstructured fluids such as polymer solutions or body fluids. Much can be accomplished in the modelling of these complex fluids by choosing a simple representation of the microstructure and considering the mechanical effect of these microstructures on the bulk fluid properties. An elastic dumbbell is an elementary physical object consisting of two spherical masses connected by a massless elastic spring. Derivations of the constitutive equation for the extra-stress tensor due to interactions between ensembles of dumbbells and an immersing solvent may be found in Owens and Phillips (2005), Bird et al. (1987), for example. In the original paper of Owens (2006) the author derived a model where Hookean dumbbells correspond to coin stack-like columns of RBC called rouleaux. Decomposing the stress tensor into viscous and elastic parts, $\sigma = 2\eta_N \dot{\gamma} + \tau$, where η_N is the plasma viscosity and τ is the contribution of the elastic dumbbells to the total (Cauchy) stress. Owens (2006) supplied full details of the derivation of the following equation for τ :

$$\tau + \mu \left(\frac{\partial \tau}{\partial t} + (u \cdot \nabla) \tau - \nabla u \cdot \tau - \tau \cdot \nabla u^T \right) = 2\eta_p \dot{\gamma}(u) \quad (3)$$

The parameter μ is the relaxation time and measures the elasticity of the fluid and the coefficient

$$\eta_p := N_0(k_B T + \kappa)\mu \quad (4)$$

is called the polymeric viscosity, due to the rouleaux. In Eq. (4), N_0 denotes the red cell number density and $k_B T + \kappa$ (having dimension J) accounts for bombardments of a rouleau by the surrounding solvent ($k_B T$) and other rouleaux (κ). k_B is the Boltzmann constant and T is the (absolute) temperature. In addition to a shear-thinning relaxation time, the essential difference between the classical Oldroyd-B model and the Owens model lies in the fact that the equilibrium length of the Hookean dumbbells in the haemorheological model change during the flow as the rouleaux aggregate and fragment. This leads to a relaxation time μ (and, therefore, a polymeric viscosity) that not only depends on the shear rate but also on the aggregate size. Thus, in addition to the constitutive equation (3) for the stress τ due to the dumbbells (rouleaux) one must also consider the evolution of the dumbbell size.

A representative equilibrium length of a dumbbell is obtained from considering the number of cells in a rouleau. A

complication is immediately seen, however, in that at any point in time and space there are rouleaux of various sizes which would have to be represented by dumbbells of various lengths and tensile properties. The simplification proposed by Owens (2006) for the computation of the elastic stress was to assume that the relaxation time μ_k for aggregates of size k is well characterised by the relaxation time μ for rouleaux of average length \hat{N} . Arguments as to why this is a reasonable simplification are given in Owens (2006). The following advection-reaction equation for \hat{N} then applies:

$$\frac{D\hat{N}}{Dt} + \frac{1}{2}b(\dot{\gamma})(\hat{N} - N_{st})(\hat{N} + N_{st} - 1) = 0 \quad (5)$$

Here $b(\dot{\gamma})$ is a fragmentation rate and $N_{st} = N_{st}(\dot{\gamma})$ is the value of \hat{N} given a steady simple shear flow with shear rate $\dot{\gamma}$. In the model of Owens (2006), the value of \hat{N} has an effect on the macroscopic elastic stress, τ in Eq. (3), via the relaxation time, μ , in the following manner:

$$\mu = \mu(\hat{N}, \dot{\gamma}) = \frac{\lambda_H \hat{N}}{1 + g_{\hat{N}} \hat{N} \lambda_H} \quad (6)$$

where $g_{\hat{N}}$ is an aggregation coefficient associated with rouleaux of \hat{N} cells, such that

$$g_{\hat{N}} \hat{N} = (1/2)b(\dot{\gamma})\hat{N}(\hat{N} - 1) + a(\dot{\gamma}) \quad (7)$$

$a(\dot{\gamma})$ is an aggregation rate for the RBC's and λ_H is the relaxation time associated with a single blood cell. In particular we would expect that at infinite shear-rates, all rouleaux would break up and therefore $\mu \rightarrow \lambda_H$ as $\dot{\gamma} \rightarrow \infty$. The assumed form for the aggregation rate $a(\dot{\gamma})$ is a piecewise cubic polynomial in $\dot{\gamma}$. The expression for $b(\dot{\gamma})$ may then be determined from considering a balance in the case of steady simple shear flow. By matching the current model with a Cross model under the assumption of a steady flow with uniform shear, η_p and N_{st} can be expressed in terms of measurable quantities. See Owens (2006) for a detailed derivation of all these coefficients.

In this paper we are solving a non-dimensional system of equations which reads as follows:

$$\left\{ \begin{array}{l} Re \frac{Du}{Dt} - 2\eta_s \nabla \cdot \dot{\gamma} - \nabla \cdot \tau + \nabla p = 0 \\ \nabla \cdot u = 0 \\ \frac{D\hat{N}}{Dt} + \frac{1}{2}b(\dot{\gamma})(\hat{N} - N_{st})(\hat{N} + N_{st} - 1) = 0 \\ \tau + De \left(\frac{\partial \tau}{\partial t} + (u \cdot \nabla) \tau - \nabla u \cdot \tau - \tau \cdot \nabla u^T \right) = 2De \dot{\gamma}(u) \end{array} \right. \quad (8)$$

Here Re is the Reynolds number and De the Deborah number, respectively defined as $\rho_f U L D e_\infty / \eta_\infty$ and $\mu U / L$. The Deborah number De varies with \hat{N} , hence the infinite shear-rate Deborah number $De_\infty = \lambda_H U / L$ is useful to characterise the flow.

2.2 Boundary conditions

In order to close the system (8), an appropriate set of boundary conditions (BCs) is required. Consider a domain Ω with boundary Γ that is split into three disjoint sets, Γ_i , Γ_o and Γ_w , respectively the inlet, outlet and wall boundaries. We denote by \mathbf{n} the outward unit normal to the boundary Γ . A main difficulty with this model is to properly set boundary conditions at the inlet. The commonly used inlet plug flow gives rise to strong singularities near the walls. Instead, a fully developed fluid flow is imposed at the inlet boundary, which fully developed flow can only be obtained by computations. However, in case of a 2-D (resp. 3-D) flow, we need to solve a 1-D (resp. 2-D) problem resulting from the system (8) restricted to the boundary Γ_i . For this problem defined on Γ_i , a constant pressure P_0 is imposed at Γ_i in the principal direction of the fluid flow, more precisely $\sigma \mathbf{n} = P_0 \mathbf{n}$. The value of P_0 can be chosen in order to impose $U_{max} = 1$. For the velocity, we will further specify no-slip conditions along the wall Γ_w . Finally along the outlet Γ_o , a mixed Dirichlet-Neumann boundary condition is used for the velocity, i.e. $\mathbf{u} \parallel \mathbf{n}$ and $\mathbf{n}^T [-p\mathbf{I} + 2\eta_s \dot{\gamma}] \mathbf{n} = 0$.

2.3 Finite element discretisation

A finite element method is used for the spatial discretisation of the above system of equations. In order to obtain a proper mixed finite element formulation, a Discrete Elastic Viscous Split Stress (DEVSS) formulation introduced in Fortin et al. (2000) is used for the discretisation of the momentum and the continuity equations. To avoid numerical instabilities due to strong convective effects, a streamline upwind Petrov-Galerkin approach is also adopted in the discretisation of the microstructure evolution and the constitutive equations (3rd and 4th equations in system (8)). We refer to Iolov et al. (2011) for a complete description of the numerical methodology.

3 NUMERICAL RESULTS

3.1 Blood flows in an aneurytic channel

In this section we discuss results obtained in an aneurytic channel under both steady and pulsatile flow conditions. This geometry mimics a blood vessel with an aneurytic formation. The configuration for this experiment is illustrated in Fig. 1. As explained in Sec. 2.2, we separate the boundary into three segments: the inlet, Γ_i ; the walls, Γ_w , and the outlet, Γ_o . At Γ_i , we impose values for \mathbf{u} , τ and \hat{N} . We solve a simplified version of the system of equations (8) for the case of an infinite channel and then apply the 1D solution as an inlet BC. On Γ_w we impose no-slip conditions on the velocity, $\mathbf{u} = 0$. At the outlet, Γ_o , we impose the natural outflow condition, $-p + 2\eta_s \partial u_x / \partial x = 0$, and no flow in the y -direction, $u_y = 0$. For our two dimensional calculations, we use the mesh shown in Fig. 2. It has 5495 triangular elements and 2916 nodes. Table 1 shows the parameter values that have been used for this test case.

3.1.1 Steady flow in an aneurytic channel

We first compute a steady flow in the aneurytic channel. The Reynolds and infinite shear-rate Deborah numbers are set, respectively, to 158 and 0.375. This steady flow will be used

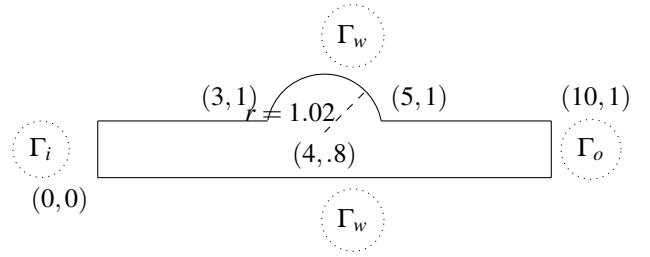


Figure 1. Flow in an aneurytic channel - geometry and boundary conditions. See the text for details.

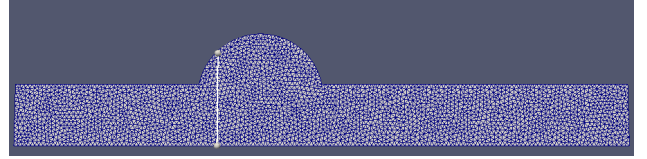


Figure 2. Mesh for the aneurytic channel. Flow variables will be plotted along the cut shown on the figure.

parameter	value	comments
η_0	0.0326	zero-shear polymeric viscosity, ($kg s^{-1} m^{-1}$)
η_∞	0.003	infinite-shear polymeric viscosity, ($kg s^{-1} m^{-1}$)
β	1.0	Cross Model coefficient
m	1	Cross Model exponent
λ_H	0.005	single cell relaxation time, (s)
η_N	0.001	plasma (Newtonian) viscosity, ($kg s^{-1} m^{-1}$)
ρ_f	1053.6	plasma fluid density, ($kg m^{-3}$)

Table 1. The model parameters used for the numerical experiment in the channel geometry. A complete description of the model parameters is given in Iolov et al. (2011).

to initiate pulsatile flow simulations in this geometry. Surface plots for flow variables can be seen in Fig. 3. Longitudinally the flow goes through three distinct sections. In the first section, between the inlet and the dilation, the flow evolves from the (viscoelastic) Poiseuille flow of an infinite straight channel. In the next section where the dilation occurs, the flow is diverted upwards to follow the geometry. In the third section, past the dilation, the flow returns to the Poiseuille flow of an infinite straight channel.

At $Re \approx 158$, the flow is well into the laminar regime and the velocity varies smoothly through the dilation, nearly symmetrically rising and falling on both sides to follow the boundary of the geometry. On the other hand the distribution of the elastic stress through the dilation is rather asymmetric. We see that the corners of the dilation have a strong effect on the elastic stress, with τ_{yy} increasing near the downstream corner, while τ_{xx} is greatest near the upstream corner.

The behaviour of \hat{N} is dictated by the local shear-rate and the flow direction. With the fluid moving upward, the distribution of \hat{N} entering the dilation from the pre-dilation channel also shifts to follow the flow. More interestingly, there is an area of quite low viscous shear, $\dot{\gamma}$, and flow stagnation

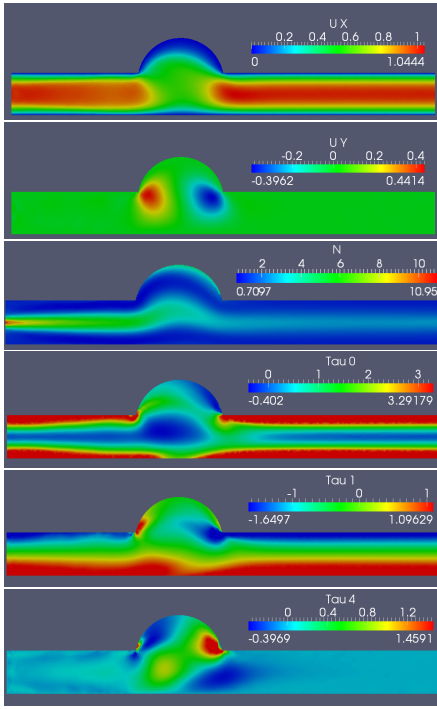


Figure 3. Steady flow in an aneurytic channel. From top to bottom, u_x , u_y , \hat{N} , τ_{xx} , τ_{xy} , τ_{yy} . $Re = 158$, $De_\infty = 0.375$.

near the upper wall of the dilation and this causes the largest values of \hat{N} to appear near that upper wall. An increase in \hat{N} implies an increase in De so, whereas on one hand we have low shear-rates and therefore low values for the components of $\dot{\gamma}$, on the other, the local Deborah number, De , is increased. In effect this results in a relatively uniform value for τ cross-sectionally within the stenosis compared to the variation in the main channel.

The effect of the dilation over the flow is quite short in space. As may be seen in Fig. 3, the velocity and rouleau size quickly reassume their profiles as in a straight channel while τ takes only slightly longer to readjust.

3.1.2 Comparisons of steady flow for various Deborah numbers Comparisons have been performed for both steady and pulsatile flows in the aneurytic channel at two different infinite shear-rate Deborah numbers, namely $De_\infty = 0.375$ and $De_\infty = 0.175$. These Deborah numbers correspond, respectively, to Reynolds numbers of 158 and 860. According to the Table I in Iolov et al. (2011), the case $De_\infty = 0.175$ (respect. $De_\infty = 0.375$) correspond to a flow at peak systole in an artery with a diameter of $0.02m$ (respect. $0.004m$). The aorta has a diameter of about $0.02m$. We see that the solution at $De_\infty = 0.375$ is more representative of blood flows in smaller arteries, at least in terms of dimensionless parameters, than the solution at $De_\infty = 0.175$. Indeed viscoelastic effects will be more prevalent with the higher De_∞ , as one expects for blood flows in small arteries. Figure 4 shows plots of four variables along the cut $x = 3.3$. The cut line is located in the aneurytic regions as indicated on Fig. 2. We only present results for the steady flows. Increasing De_∞ results in

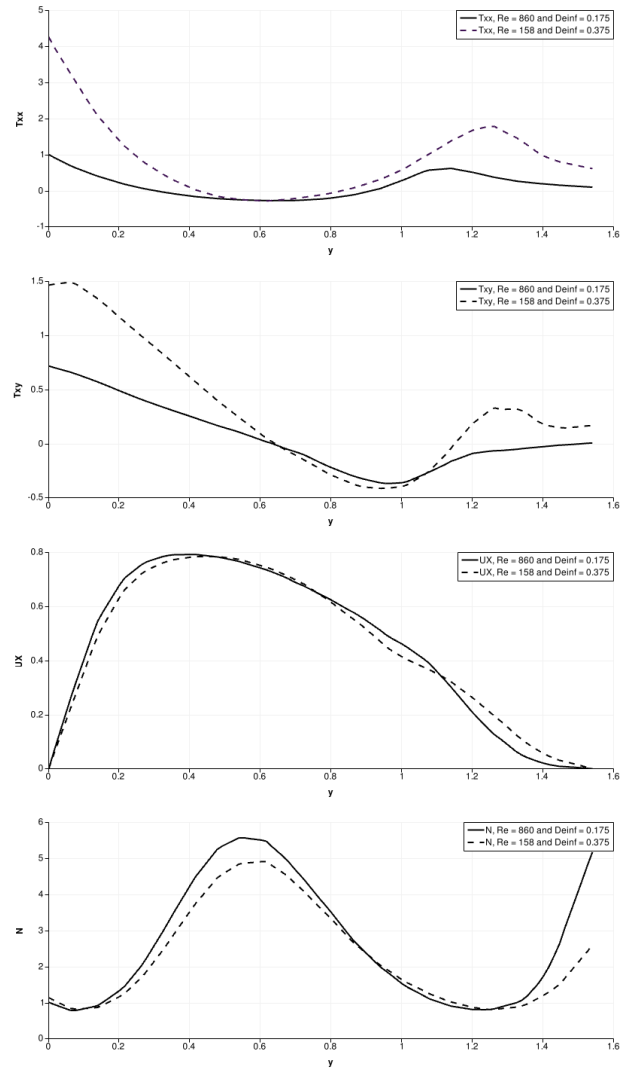


Figure 4. Effect of the Deborah number on the aneurytic channel flow. The variables are plotted along a cross-sectional cut at $x = 3.3$. From top-to-bottom: τ_{xx} , τ_{xy} , u_x and \hat{N} .

smaller rouleaux in the center of the channel and near the wall in the aneurytic bump, but in larger extra-stresses τ_{xx} and τ_{xy} (also true for τ_{yy} but not shown here). These extra-stresses can be up to 3-4 times larger for the higher De_∞ with the largest deviations on the extra-stresses seen near the lower wall and in the middle of the aneurytic bump. The velocity fields deviate from each other, but the magnitude of the difference between velocities is considerably smaller than for the extra-stresses.

3.1.3 Pulsatile blood flow in an aneurytic channel We now present results obtained in the aneurytic channel under pulsatile flow conditions. The steady solution obtained in Sec. 3.1.1 is used as initial condition for the pulsatile simulations. Computations have been performed for two test cases, one where $De_\infty = 0.375$ and $Re = 158$ and the other with $De_\infty = 0.175$ and $Re = 860$. For our physical frequency we have chosen a physiologically reasonable value of 60 heart

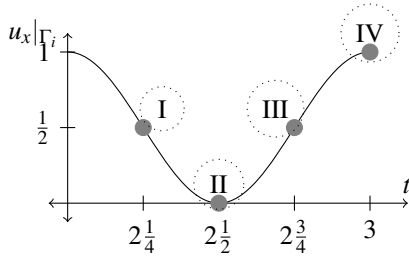


Figure 5. Observation times for pulsatile flows

beats per minutes, corresponding to a non-dimensional frequency of 0.05. A hundred time-steps are computed per period over three heart beats.

The points in time during the cycle when we show the variables are illustrated in Fig. 5. Time *I* corresponds to peak deceleration, time *II* to the minimal inflow velocity (peak diastole), time *III* to peak acceleration and time *IV* to maximum inflow velocity (peak systole). Snapshots of the flow variables during a single cycle over these four equally spaced time intervals can be seen in Figs. 6–8. These are taken from the last (third) cycle of the simulation. The pressure p is not shown since it essentially decreases linearly along the length of the domain. We show u and \hat{N} only for the flow at $De_\infty = 0.375$. These variables look very similar for $De_\infty = 0.175$. On the other hand, comparing Figs. 7 and 8, one notices that the extra-stresses τ are larger over larger regions for the larger Deborah number, and this for the whole cycle except maybe at peak diastole. This is consistent with what was observed in the steady case.

A few things are notable when looking at the pulsatile solution. At these low Reynolds numbers, we have a lot of damping on the fluid and thus there is almost no flow at peak diastole, time *II*. At peak systole, time *IV*, we have a lot of shear which generates large values for the components of τ .

The solutions for u are quite symmetric in time around the middle of a cycle. That is, u behaves in the same way during the deceleration (time *I*) as it does during the acceleration (time *III*), as can be seen by comparing respective surface plots. This is only partially true for the stresses τ with spatial variations of stresses being milder and more spread out at time *III* (following diastole) than time *I*.

What is interesting is that while u and τ both oscillate in time due to the pulsatility, \hat{N} shows little variation over time. A similar behaviour was observed in the time-dependent simulations in the original papers (Owens, 2006; Fang and Owens, 2006), and we see that again here. Our initial conditions correspond to peak systole and correspondingly a low value for the average rouleau size across the domain. Even though during each pulse cycle the shear is reduced, the time-scales inherent in the parameter values for \hat{N} imply that there is not enough time in this flow regime for the RBC's to aggregate into larger rouleaux. Therefore \hat{N} remains relatively constant over time despite the relatively large oscillations in u and $\dot{\gamma}$.

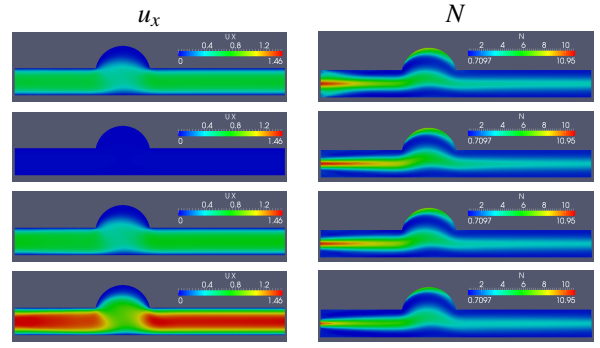


Figure 6. Horizontal velocity u_x (left) and average rouleau size \hat{N} (right), at times *I* - *IV* (from top to bottom) of the pulsating test case. $Re = 158$, $De_\infty = 0.375$.

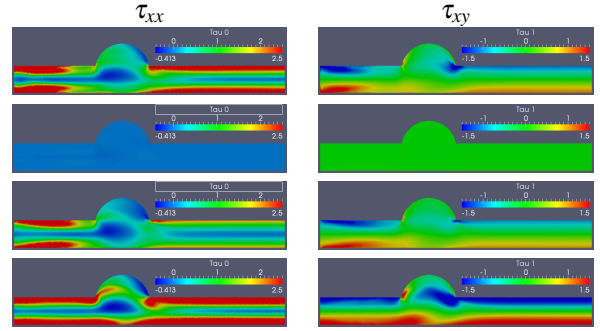


Figure 7. τ_{xx} (left) and τ_{xy} (right), at times *I* - *IV* (from top to bottom) of the pulsating test case. $Re = 158$, $De_\infty = 0.375$.

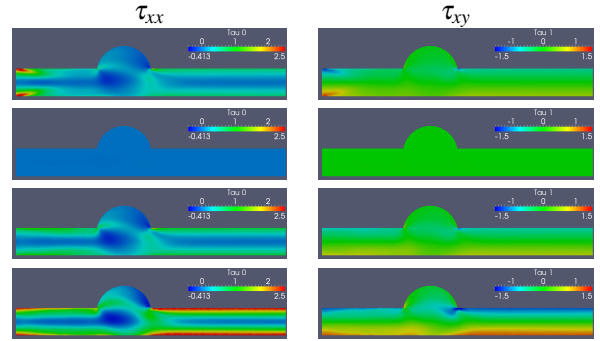


Figure 8. τ_{xx} (left) and τ_{xy} (right), at times *I* - *IV* (from top to bottom) of the pulsating test case. $Re = 860$, $De_\infty = 0.175$.

3.2 Three-dimensional fluid flow in a carotid bifurcation

We now show a 3-D Newtonian flow in a human carotid artery bifurcation geometry that will serve as a comparison test case for the non-Newtonian flow. This test case is inspired and uses the geometry from Vétel et al. (2009). The flow is steady at a Reynolds number of 1000 based on the inlet diameter and maximal velocity. Figure 9 shows the geometry and flow features near the main bifurcation between the left and right carotid artery. One can see that a secondary flow is induced near the main bifurcation, with strong vorticity especially in the left branch. The comparison with the

corresponding non-Newtonian flow will be most interesting.

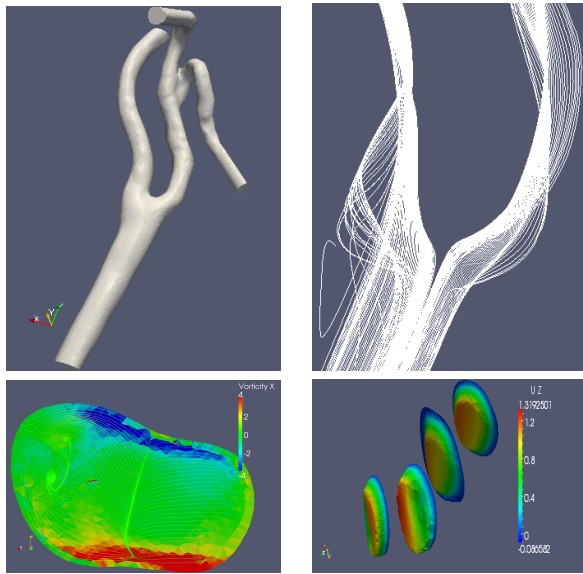


Figure 9. Geometry of the carotid artery bifurcation (top left), streamlines near the main bifurcation (top right), surface plot of the vorticity superposed with in-plane streamlines on a cut plane upstream the main bifurcation (bottom left) and profiles of the vertical velocity u_z on three horizontal cut planes upstream and downstream the main bifurcation (bottom right).

4 CONCLUSIONS

This work sets up the framework for the numerical, in particular finite element, solution of microstructure-based, Oldroyd-B type models for blood. Following the zero-dimensional computations in Owens (2006) and the one-dimensional oscillatory flow simulations in Fang and Owens (2006), we were able to employ the finite element method to perform two-dimensional steady and pulsatile flow simulations in a non-trivial geometry (our aneurysmic channel). Using physiologically plausible values for the model's parameters in this geometry we made a comparison of flows for two sets of Reynolds and Deborah numbers, with flow conditions and sizes corresponding to arteries with a diameter of $0.02m$ and $0.004m$. We managed to compute flows for these Reynolds and Deborah numbers by replacing the plug flow inlet boundary conditions that were used in Iolov et al. (2011) by boundary conditions obtained from solving a 1-D problem. This results in a major improvement in the robustness of our finite element method

As expected, viscoelastic effects were stronger in the smaller artery. Elastic stresses were still relatively important in the larger artery, which is about the size of the aorta. Other non-Newtonian models (e.g. Casson's model, the Herschel-Buckley fluid model, the Carreau-Yasuda model, power-law

fluids and the Quemada model) predicted limited differences with Newtonian flows in similar aneurysmic geometries. All these models deduce shear stresses from local strains, while RBC rouleaux that control the blood viscoelastic properties are advected by the flow leading to a non-local viscoelastic response of the blood. However our results indicate that the combination of viscoelastic, shear-thinning, hysteresis and non-local effects in the determination of the blood viscosity and stresses results in a more dominant non-Newtonian behaviour of blood. These effects must be accounted for to properly model the rheological properties of blood. This may call into question the validity of performing Newtonian flow simulations even in large arteries such as the aorta in pathological cases.

Finally a test case for three-dimensional flow comparison has been identified, with computations of the non-Newtonian flow well under way.

ACKNOWLEDGEMENTS

This work was supported by a National Science and Engineering Research Council (NSERC) Discovery Grant and a Postdoctoral Scholarship from the Centre de Recherches Mathématiques (CRM) to the first author.

REFERENCES

- Bird, R.B., Curtiss, C.F., Armstrong, R.C., and Hassager, O., 1987, "Dynamics of Polymeric Liquids, Vol. 2, Kinetic Theory", John Wiley & Sons, New York.
- Fang, J., and Owens, R.G., 2006, "Numerical simulations of pulsatile blood flow using a new constitutive model", *Biorheology*, 43: 637–660.
- Fortin, M., Guénette, R., and Pierre R., 1997, "Numerical analysis of the modified EVSS method", *Computer Methods in Applied Mechanics and Engineering*, 143: 79–95.
- Fortin, A., Guénette, R., and Pierre, R., 2000, "On the discrete EVSS method", *Computer Methods in Applied Mechanics and Engineering*, 189: 121–139.
- Guénette, R., and Fortin, M., 1995, "A new mixed finite element method for computing viscoelastic flows", *Journal of Non-Newtonian Fluid Mechanics*, 60: 27–52.
- Iolov, A, Kane, A.S., Bourgault, Y., Owens, R.G. and Fortin, A., 2011, "A FEM for a microstructure-based model of blood", *Commun. Numer. Meth. Engng*, in press.
- Moyers-Gonzalez, M., Owens, R.G., and Fang, J., 2008, "A non-homogeneous constitutive model for human blood Part III. Oscillatory flow", *Journal of Non-Newtonian Fluid Mechanics*, 155: 161–173.
- Owens, R.G., and Phillips, T.N., 2005, "Computational Rheology", Imperial College Press, London.
- Owens, R.G., 2006, "A new microstructure-based constitutive model for human blood", *Journal of Non-Newtonian Fluid Mechanics*, 140: 57–70.
- Vétel, J., Garon, A., and Pelletier, D., 2009, "Lagrangian coherent structures in the human carotid artery bifurcation", *Exp. Fluids*, 46: 1067–1079.